

See discussions, stats, and author profiles for this publication at: <https://www.researchgate.net/publication/258640404>

Different Upconversion Properties of β -NaYF₄:Yb³⁺,Tm³⁺/Er³⁺ in Affecting the Near-Infrared-Driven Photocatalytic Activity of High-Reactive TiO₂

ARTICLE in ACS APPLIED MATERIALS & INTERFACES · NOVEMBER 2013

Impact Factor: 6.72 · DOI: 10.1021/am404389g · Source: PubMed

CITATIONS

19

READS

149

5 AUTHORS, INCLUDING:



Wei Wang

Chinese Academy of Sciences

1,002 PUBLICATIONS 11,195 CITATIONS

[SEE PROFILE](#)



Wenjuan Huang

Nanjing University of Technology

14 PUBLICATIONS 108 CITATIONS

[SEE PROFILE](#)



Yaru Ni

Nanjing University of Technology

90 PUBLICATIONS 596 CITATIONS

[SEE PROFILE](#)

Different Upconversion Properties of $\beta\text{-NaYF}_4:\text{Yb}^{3+},\text{Tm}^{3+}/\text{Er}^{3+}$ in Affecting the Near-Infrared-Driven Photocatalytic Activity of High-Reactive TiO_2

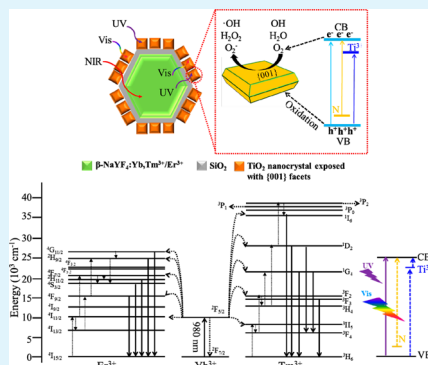
Wei Wang,* Wenjuan Huang, Yaru Ni, Chunhua Lu,* and Zhongzi Xu

State Key Laboratory of Materials-Orient Chemical Engineering, College of Materials Science and Engineering, Nanjing University of Technology, Nanjing, Jiangsu 210009, PR China

Supporting Information

ABSTRACT: Double-shell-structured $\beta\text{-NaYF}_4:\text{Yb}^{3+},\text{Tm}^{3+}/\text{Er}^{3+}@\text{SiO}_2@\text{TiO}_2$ upconversion photocatalysts have been successfully synthesized by a simple hydrothermal method. It is found that the double-shell-structured photocatalyst consists of uniform $\beta\text{-NaYF}_4:\text{Yb}^{3+},\text{Tm}^{3+}/\text{Er}^{3+}$ nanocrystals, SiO_2 as the media shell, and anatase TiO_2 nanocrystals exposed with the high-reactive {001} facets as the outer shell. The TiO_2 shell is modified to absorb both the UV and visible light in order to make sufficient use of the upconverted light from $\beta\text{-NaYF}_4:\text{Yb}^{3+},\text{Tm}^{3+}/\text{Er}^{3+}$ for photocatalysis. Effective energy transfer from $\beta\text{-NaYF}_4:\text{Yb}^{3+},\text{Tm}^{3+}/\text{Er}^{3+}$ to TiO_2 and its importance are confirmed. The photocatalytic activity in the degradation of Rhodamine B (RhB) under the near-infrared (NIR) (980 nm laser) irradiation suggests that the NIR-driven photocatalytic activity of the double-shell-structured photocatalyst is significantly dependent on the properties of the upconversion materials and the irradiated NIR power density. Moreover, the NIR-driven photocatalyst shows stable photocatalytic degradation of RhB in the recycled tests. This study suggests a promising system and a new insight to understand the application of appropriate upconversion materials to effectively utilize the NIR for photocatalytic applications of TiO_2 -based photocatalysts, which may advance the application of solar energy in the future.

KEYWORDS: upconversion, photocatalysis, TiO_2 , core–shell structure, NaYF_4



1. INTRODUCTION

In recent years, water and air pollution has become a serious problem and has attracted great attention all over the world.^{1,2} Since Fujishima and Honda discovered the hydrogen production phenomenon on the TiO_2 electrode in 1972, the use of the semiconductor TiO_2 photocatalyst has grown significantly due to its chemical stability, environmental friendliness, and strong oxidation ability under the UV irradiation.^{3–5} However, the UV only occupies ca. 5% of the solar energy; the rest of the energy in the visible (ca. 48%) and near-infrared (NIR) (ca. 47%) range is not used sufficiently for photocatalysis.⁶ As a result, large scale practical application of TiO_2 -based photocatalysts to solve environmental and energy problems needs further innovative work.

In order to extend the limited optical absorption edge of TiO_2 , persistent efforts have been done by researchers to adjust the light absorption edge toward the visible and even NIR range, for instance, employing metal or nonmetal impurities to generate acceptor or donor states in the band gap, self-doping by Ti^{3+} and oxygen vacancies, depositing noble metals, coupling with semiconductors, and modifying with carbon-based materials.^{7–14} It is true that the light absorption edge can be extended to the long wavelength range (mostly visible light range) with the help of these strategies, but efficient NIR

absorption for photocatalysis is still unreached yet. Recently, it has been reported that hydrogenation of anatase TiO_2 nanocrystals can extend the light absorption edge to ca. 1200 nm by forming a disorder structure in the crystal lattice.¹⁵ However, this point still needs systematic investigation because no further experimental studies by other researchers have confirmed this result. Hence, the incapacity of utilizing the NIR has become one of the principal factors limiting the large scale industrial application of TiO_2 -based photocatalysts.

To overcome this limitation, upconversion phosphors (UCPs), which can transform NIR photons to UV and vis photons, have been considered as one of the most promising solutions and have already been applied in photocatalysis and solar cells.^{16–18} According to the reported in situ works, UCPs were mainly physically mixed with the semiconductor photocatalysts.¹⁹ This strategy truly gives a new insight in employing the UCPs for photocatalysis. However, the energy transfer efficiency was low due to the loose contact between the UCPs and photocatalyst. The as-prepared photocatalysts even cannot disperse well in aqueous solutions for water purification due to

Received: October 6, 2013

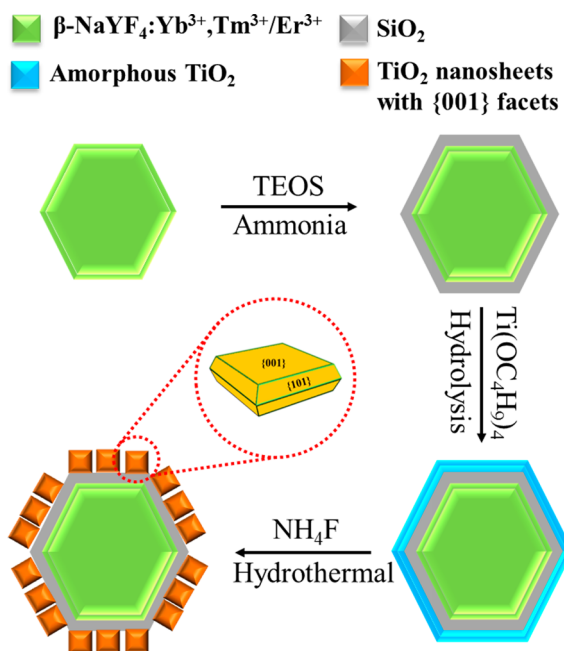
Accepted: November 18, 2013

Published: November 18, 2013

the hydrophobic properties of the UCPs.²⁰ The wide bandgap and low reactivity of the photocatalysts determine that the photocatalytic activities of these upconversion photocatalytic composites in aqueous solution were enhanced by only a small fraction.^{16,17} Moreover, the influence of different upconversion properties of the UCPs in affecting the NIR-driven photocatalysis is still unreported yet.

In this work, we designed a uniform double-shell-structured photocatalyst, which can effectively harvest the NIR for photocatalysis, for the first time. It consisted of β -NaYF₄:Yb³⁺,Tm³⁺/Er³⁺ as the core, amorphous SiO₂ as the media shell, and UV-vis responsive high-reactive anatase TiO₂ nanocrystals exposed with the {001} facets as the outer shell (Scheme 1). To confirm the influence of different UCPs played

Scheme 1. Schematic Illustration for the Preparation of β -NaYF₄:Yb³⁺,Tm³⁺/Er³⁺@SiO₂@TiO₂ Double-Shell-Structured Upconversion Photocatalysts^a



^aThe TiO₂ shell is composed of anatase nanocrystals exposed with the {001} facets.

on photocatalysis, β -NaYF₄ sensitized by Yb³⁺ and activated by Tm³⁺ or Er³⁺ ions, which will emit blue and green light (different photon energy), respectively, was introduced. Results indicate that the as-prepared photocatalyst presented a high performance for Rhodamine B (RhB) degradation under the NIR irradiation with the help of suitable UCPs (β -NaYF₄:Yb³⁺,Tm³⁺) and a proper structure for efficient energy transfer. This work will give a new sight to understand the effect of different upconversion properties on enhancing the NIR-driven photocatalytic activity of TiO₂-based photocatalysts.

2. EXPERIMENTAL SECTION

2.1. Preparation of β -NaYF₄:Yb³⁺,Tm³⁺/Er³⁺ Nanoparticles. Monodispersed β -NaYF₄:Yb³⁺,Tm³⁺ nanoparticles were synthesized according to the methods reported before. Typically, 20 mL of 1-octadecene along with 20 mL of oleic acid were added into a 100 mL 3-necked flask containing 2 mmol of YCl₃·6H₂O and a small amount of YbCl₃·6H₂O and TmCl₃·6H₂O (molar ratio of YCl₃·6H₂O/YbCl₃·6H₂O/TmCl₃·6H₂O was 79.5:20:0.5). The mixture was heated to 156 °C under the N₂ atmosphere and held at that temperature for 30 min. The obtained solution was cooled down to 60 °C. Then, a 20 mL methanol solution containing 8 mmol of NH₄F and 5 mmol of NaOH was added dropwise. The resulting solution was stirred at the initial temperature for 30 min to consume all the fluoride and then slowly heated to 100 °C and maintained for 10 min to evaporate the methanol. At last, the flask was heated to 310 °C and held at this temperature for 60 min under the N₂ atmosphere. After the mixture cooled down to room temperature, the obtained nanoparticles were precipitated by adding 20 mL of ethanol and were separated by centrifugation. The washed nanoparticles were dried at 60 °C in vacuum overnight. For the preparation of β -NaYF₄:Yb³⁺,Er³⁺, TmCl₃·6H₂O was replaced by ErCl₃·6H₂O and the molar ratio of YCl₃·6H₂O/YbCl₃·6H₂O/ErCl₃·6H₂O was 78:20:2. The rest of the procedures were the same as that for the preparation of β -NaYF₄:Yb³⁺,Tm³⁺.

2.2. Preparation of β -NaYF₄:Yb³⁺,Tm³⁺/Er³⁺@SiO₂@TiO₂ Photocatalysts. In a typical synthesis procedure, 0.19 g of β -NaYF₄:Yb³⁺,Tm³⁺ was suspended in 200 mL of isopropyl alcohol by sonication and magnetic stirring. Then, 10 mL of deionized water and 6 mL of ammonium hydroxide (volume concentration of ca. 25%) were added into the suspension, followed by magnetic stirring for 20 min; 0.41 g of tetraethyl orthosilicate (TEOS) was added into 20 mL of isopropyl alcohol to form a transparent solution which will be added into the aforementioned suspension with a dropping speed of 1 mL/min by a peristaltic pump. The mixture was magnetically stirred at room temperature for 6 h to obtain SiO₂ coated β -NaYF₄:Yb³⁺,Tm³⁺. The as-prepared sample, named β -NaYF₄:Yb³⁺,Tm³⁺@SiO₂, was dried at 60 °C overnight.

β -NaYF₄:Yb³⁺,Tm³⁺@SiO₂ (0.2 g) was dispersed in 20 mL of alcohol by sonication treatment. Then, 0.1 g of hydroxypropyl cellulose and 0.1 mL of deionized water were added into the suspension, followed by magnetic stirring for 2 h at room temperature to ensure the sufficient adsorption of hydroxypropyl cellulose by β -NaYF₄:Yb³⁺,Tm³⁺@SiO₂. One milliliter of tetrabutyl titanate was added into 5 mL of alcohol to form a transparent solution which was then added into the suspension with a speed of 0.5 mL/min by the peristaltic pump. After injection, the temperature was increased to 85 °C under refluxing conditions for 100 min. The precipitate was isolated by centrifugation, washed with ethanol, and dispersed in 33 mL of ethanol to give a β -NaYF₄:Yb³⁺,Tm³⁺@SiO₂@amorphous TiO₂ suspension.

The as-obtained β -NaYF₄:Yb³⁺,Tm³⁺@SiO₂@amorphous TiO₂ suspension was mixed with 17 mL of deionized water containing 0.09 g of NH₄F by sonication and magnetic stirring for 30 min. The resulting suspension was transferred to a dried Teflon-lined stainless steel autoclave with a capacity of 60 mL, which will be heated at 180 °C for 24 h in an electric oven. After the reaction, the yellow-colored product was washed with deionized water and ethanol for three times to remove the residual contamination by centrifugation. The finally obtained product, named β -NaYF₄:Yb³⁺,Tm³⁺@SiO₂@TiO₂, was dried at 60 °C in a vacuum oven. For the preparation of β -NaYF₄:Yb³⁺,Er³⁺@SiO₂@TiO₂ double-shell-structured photocatalyst, β -NaYF₄:Yb³⁺,Tm³⁺ was replaced by β -NaYF₄:Yb³⁺,Er³⁺ and the rest of the processes were the same. With the help of the above experimental method, the obtained molar ratio of TiO₂ to β -NaYF₄:Yb³⁺,Tm³⁺/Er³⁺ was 2.7:1 in the finally obtained upconversion photocatalysts. Pure TiO₂ nanocrystals were also prepared by the same method in the absence of β -NaYF₄:Yb³⁺,Tm³⁺/Er³⁺@SiO₂.

2.3. Preparation of Physical Mixtures of P25/TiO₂ and β -NaYF₄:Yb³⁺,Tm³⁺/Er³⁺. Commercial P25 (Degussa, Germany) is a well-known UV responsive TiO₂ photocatalyst. The combination of P25 with β -NaYF₄:Yb³⁺,Tm³⁺/Er³⁺ can be used to confirm the upconverted UV in driving the photocatalytic reaction. Typically, 0.1 g of P25 and 0.1 g of β -NaYF₄:Yb³⁺,Tm³⁺/Er³⁺ were mixed together by dry ball milling with a speed of 250 rpm. The physical mixtures, named β -NaYF₄:Yb³⁺,Tm³⁺/P25 and β -NaYF₄:Yb³⁺,Er³⁺/P25, were collected for photocatalytic activity measurement. The same process was also used to prepare β -NaYF₄:Yb³⁺,Tm³⁺/TiO₂ and β -NaYF₄:Yb³⁺,Er³⁺/TiO₂.

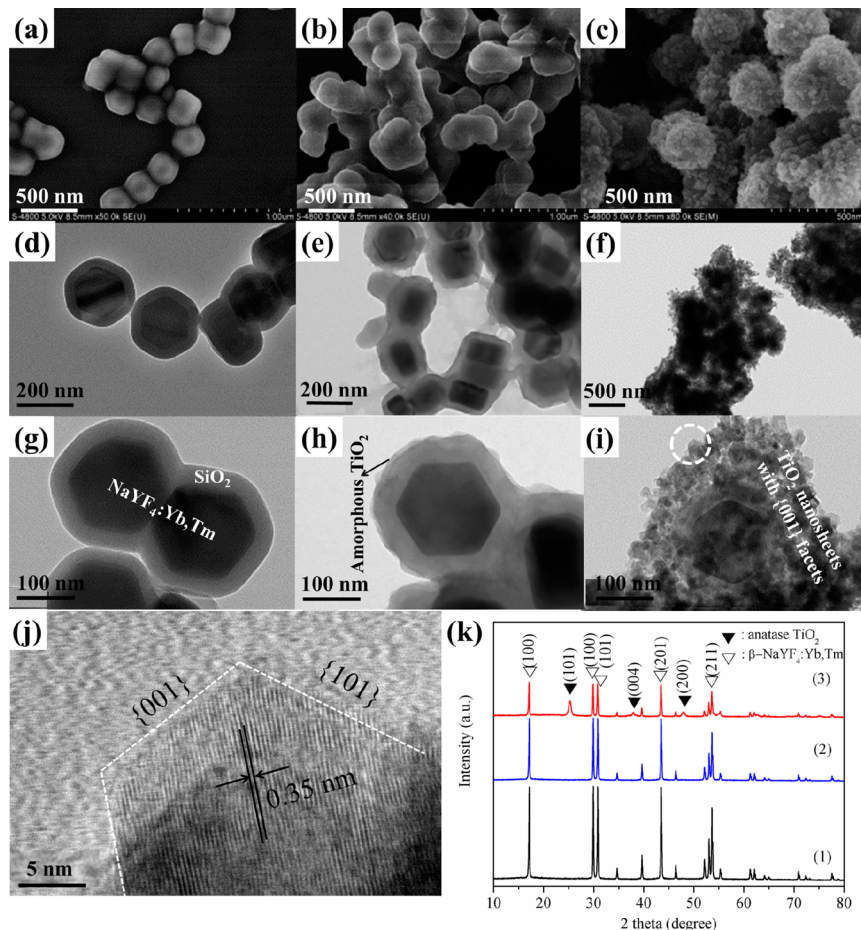


Figure 1. SEM and TEM images of (a, d, g) $\beta\text{-NaYF}_4\text{:Yb}^{3+}\text{,Tm}^{3+}\text{@SiO}_2$, (b, e, h) $\beta\text{-NaYF}_4\text{:Yb}^{3+}\text{,Tm}^{3+}\text{@SiO}_2\text{@amorphous TiO}_2$, and (c, f, i) $\beta\text{-NaYF}_4\text{:Yb}^{3+}\text{,Tm}^{3+}\text{@SiO}_2\text{@TiO}_2$ show the fabrication processes and structures of $\beta\text{-NaYF}_4\text{:Yb}^{3+}\text{,Tm}^{3+}$ -based double-shell-structured upconversion photocatalysts. (j) High resolution TEM image of the nanoparticle circled in panel i confirms the TiO_2 shell is composed of nanocrystals exposed with the $\{001\}$ facets. (k) XRD patterns of (1) $\beta\text{-NaYF}_4\text{:Yb}^{3+}\text{,Tm}^{3+}$, (2) $\beta\text{-NaYF}_4\text{:Yb}^{3+}\text{,Tm}^{3+}\text{@SiO}_2$, and (3) $\beta\text{-NaYF}_4\text{:Yb}^{3+}\text{,Tm}^{3+}\text{@SiO}_2\text{@TiO}_2$ show the crystal phase of anatase TiO_2 and $\beta\text{-NaYF}_4\text{:Yb}^{3+}\text{,Tm}^{3+}$.

2.4. Characterization. Powder X-ray diffraction (XRD) measurements of as-prepared samples were conducted on an ARL X'TRA X-ray diffractometer using Cu K α radiation ($\lambda = 0.15406$ nm) at a scanning rate of 5°/min. During the measurement process, the voltage was set as 40 kV, electric current was 30 mA, and the step width was 0.02°. An UV-vis light absorption spectrum was obtained with a 3101 spectrophotometer with BaSO₄ as the reference sample. Scanning electron microscopy (SEM) was performed with a S-4800 scanning electron analyzer with an accelerating voltage of 15 kV. Transmittance electron microscopy (TEM) analysis was conducted on a JEM-2010 electron microscope (JEOL, Japan) at an accelerating voltage of 200 kV. Each sample (0.2 g) was compressed in a mold with the same pressure in order to record the photoluminescence (PL) emission spectrum on a FL3-221 fluorescence spectrophotometer with a 980 nm laser as the excitation source at room temperature. As the light flux of each sample was the same, the obtained emission bands of each sample can compare the intensity with each other. The surface chemical environments were analyzed by X-ray photoelectron spectra (XPS) on a PHI5000 VersaProbe system with monochromatic Al K α X-rays. All the peaks were calibrated with the contaminated C 1s peak of 284.6 eV. Electron paramagnetic resonance (EPR) spectra were recorded on a Bruker EMX 10/12 spectrometer (X-band) equipped with a cylindrical cavity operating with a microwave frequency of 9.3503 GHz. The sample (100 mg) was cooled to 77 K using liquid He. The magnetic field was measured by means of a Bruker ER035 M NMR gaussmeter.

2.5. Photocatalytic Activity of As-Prepared Photocatalysts.

Photocatalytic reaction was performed by monitoring the RhB

degradation. The concentration change was estimated by measuring the optical absorption peak at 553 nm using the Shimadzu UV-3101 spectrophotometer. In a typical experiment, 10 mg of as-prepared photocatalysts was dispersed into a quartz bottle containing 10 mL of RhB aqueous solution (10^{-5} M) and then kept stirring in the dark for 1 h to establish the adsorption-desorption equilibrium between RhB and the photocatalyst. A 980 nm laser with different power density (3, 7, 10, and 15 W/mm²) was used as the light source for the NIR-driven photocatalytic reaction. After irradiation for a designated time, 0.5 mL of the RhB aqueous solution was taken out to measure the absorption spectrum and then put back into the quartz bottle for further measurement. In order to investigate the photocatalytic activity under the UV and visible light irradiation, a 14 W UV lamp with central peak at 365 nm and a 500 W xenon lamp covered with an UV filter were also used as the light source.

3. RESULTS AND DISCUSSION

3.1. Crystal Structure and Morphology. The SEM images of $\beta\text{-NaYF}_4\text{:Yb}^{3+}\text{,Tm}^{3+}$ and $\beta\text{-NaYF}_4\text{:Yb}^{3+}\text{,Er}^{3+}$ are presented in Figure S1, Supporting Information. As can be seen, both the uniform and monodispersed UCPs have a particle size of ca. 150 nm in diameter and ca. 100 nm in height. No distinguishable differences in morphology were detected between the two UCPs, indicating that different doping processes have little influence on the morphology features.²¹ As a result, we employ $\beta\text{-NaYF}_4\text{:Yb}^{3+}\text{,Tm}^{3+}$ -based samples to

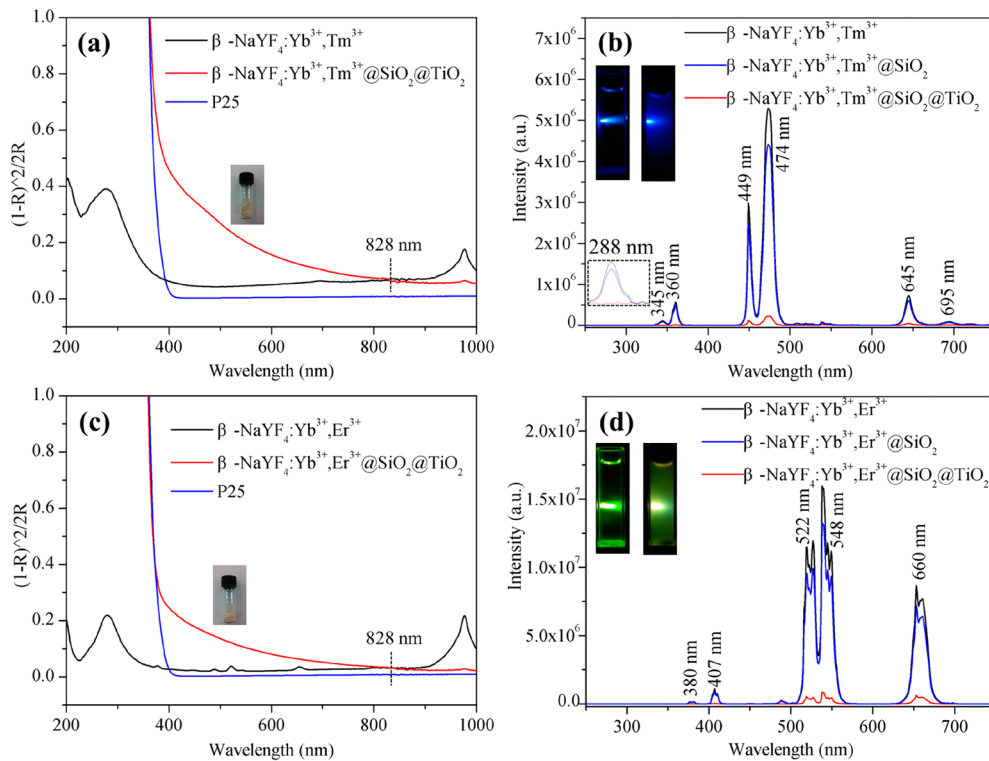


Figure 2. UV-vis light absorption spectra of (a) $\beta\text{-NaYF}_4\text{:Yb}^{3+},\text{Tm}^{3+}$, $\beta\text{-NaYF}_4\text{:Yb}^{3+},\text{Tm}^{3+}@\text{SiO}_2@\text{TiO}_2$, and P25 and (c) $\beta\text{-NaYF}_4\text{:Yb}^{3+},\text{Er}^{3+}$, $\beta\text{-NaYF}_4\text{:Yb}^{3+},\text{Er}^{3+}@\text{SiO}_2@\text{TiO}_2$, and P25. The true colors of $\beta\text{-NaYF}_4\text{:Yb}^{3+},\text{Tm}^{3+}@\text{SiO}_2@\text{TiO}_2$ and $\beta\text{-NaYF}_4\text{:Yb}^{3+},\text{Er}^{3+}@\text{SiO}_2@\text{TiO}_2$ are also inserted in (a) and (c), respectively. Photoluminescence spectra of (b) $\beta\text{-NaYF}_4\text{:Yb}^{3+},\text{Tm}^{3+}$, $\beta\text{-NaYF}_4\text{:Yb}^{3+},\text{Tm}^{3+}@\text{SiO}_2$, and $\beta\text{-NaYF}_4\text{:Yb}^{3+},\text{Tm}^{3+}@\text{SiO}_2@\text{TiO}_2$ and (d) $\beta\text{-NaYF}_4\text{:Yb}^{3+},\text{Er}^{3+}$, $\beta\text{-NaYF}_4\text{:Yb}^{3+},\text{Er}^{3+}@\text{SiO}_2$, and $\beta\text{-NaYF}_4\text{:Yb}^{3+},\text{Er}^{3+}@\text{SiO}_2@\text{TiO}_2$. The actual photoluminescence images of $\beta\text{-NaYF}_4\text{:Yb}^{3+},\text{Tm}^{3+}$ and $\beta\text{-NaYF}_4\text{:Yb}^{3+},\text{Er}^{3+}$ dispersed in cyclohexane and $\beta\text{-NaYF}_4\text{:Yb}^{3+},\text{Tm}^{3+}@\text{SiO}_2@\text{TiO}_2$ and $\beta\text{-NaYF}_4\text{:Yb}^{3+},\text{Er}^{3+}@\text{SiO}_2@\text{TiO}_2$ dispersed in deionized water are shown on the left (inset) and right (inset) of (b) and (d), respectively.

illustrate the morphology changes during the further experimental process.

After coating $\beta\text{-NaYF}_4\text{:Yb}^{3+},\text{Tm}^{3+}$ with SiO_2 (Figure 1a), amorphous TiO_2 (Figure 1b), and TiO_2 nanocrystals exposed with the $\{001\}$ facets (Figure 1c), it can be clearly observed that the surface structure was changed significantly. In addition, we noticed that coating with SiO_2 and TiO_2 will induce slight aggregation between the particles, as can be seen from the TEM images shown in Figure 1d–f. In Figure 1g, it is clear that the surface of $\beta\text{-NaYF}_4\text{:Yb}^{3+},\text{Tm}^{3+}@\text{SiO}_2$ is very smooth and the thickness of SiO_2 is ca. 30 nm. When TiO_2 was introduced onto the surface of $\beta\text{-NaYF}_4\text{:Yb}^{3+},\text{Tm}^{3+}@\text{SiO}_2$ (Figure 1h,i), the double-shell structure of SiO_2 and TiO_2 can be observed clearly. The outer TiO_2 shell is composed of a large amount of nanocrystals with a size of ca. 20 nm. These TiO_2 nanocrystals will result in a large internal surface area so as to enhance the contact with water contaminants for efficient photocatalytic degradation.⁷

To verify the crystal structure of as-obtained TiO_2 nanocrystals, the high resolution TEM image shown in Figure 1j gives fine-resolved lattice fringes of the nanocrystal circled in Figure 1i. The interplanar distance between adjacent lattice planes was determined as ca. 0.35 nm, matching the $d(101)$ value of anatase TiO_2 .^{22,23} Combining the typical shape of the nanocrystal, we can deduce that the TiO_2 nanocrystal is exposed with the high-reactive $\{001\}$ facets. This crystal structure will enhance the photocatalytic activity compared to the nanocrystals dominated by the more thermodynamic stable $\{101\}$ facets.^{24,25} Figure 1k shows the XRD patterns of as-synthesized $\beta\text{-NaYF}_4\text{:Yb}^{3+},\text{Tm}^{3+}$, $\beta\text{-NaYF}_4\text{:Yb}^{3+},\text{Tm}^{3+}@\text{SiO}_2$,

and $\beta\text{-NaYF}_4\text{:Yb}^{3+},\text{Tm}^{3+}@\text{SiO}_2@\text{TiO}_2$. Major XRD peaks of the three samples can be indexed to $\beta\text{-NaYF}_4$ (JCPDS No. 16-0334).²¹ The typical diffraction peaks of anatase TiO_2 detected in $\beta\text{-NaYF}_4\text{:Yb}^{3+},\text{Tm}^{3+}@\text{SiO}_2@\text{TiO}_2$ confirms the presence of TiO_2 and previous crystal structure analysis. Due to the coating with SiO_2 and TiO_2 layers, the relative diffraction intensity of $\beta\text{-NaYF}_4\text{:Yb}^{3+},\text{Tm}^{3+}$ in $\beta\text{-NaYF}_4\text{:Yb}^{3+},\text{Tm}^{3+}@\text{SiO}_2$ and $\beta\text{-NaYF}_4\text{:Yb}^{3+},\text{Tm}^{3+}@\text{SiO}_2@\text{TiO}_2$ was slightly weakened compared to that of pure $\beta\text{-NaYF}_4\text{:Yb}^{3+},\text{Tm}^{3+}$. Similar double-shell structures and XRD patterns were also observed for $\beta\text{-NaYF}_4\text{:Yb}^{3+},\text{Er}^{3+}$ -based samples (Figures S2 and S3, Supporting Information).

3.2. Optical Properties. UV-vis light absorption spectra of $\beta\text{-NaYF}_4\text{:Yb}^{3+},\text{Tm}^{3+}@\text{SiO}_2@\text{TiO}_2$, $\beta\text{-NaYF}_4\text{:Yb}^{3+},\text{Tm}^{3+}$ and P25 are shown in Figure 2a. Compared to the spectrum of $\beta\text{-NaYF}_4\text{:Yb}^{3+},\text{Tm}^{3+}$, it is obvious that the yellow colored $\beta\text{-NaYF}_4\text{:Yb}^{3+},\text{Tm}^{3+}@\text{SiO}_2@\text{TiO}_2$ (inset in Figure 2a) also shows a light absorption peak at 980 nm, which is the typical property of Yb^{3+} . More importantly, a light absorption edge before 400 nm which is overlapped with that of P25, corresponding to the band absorption of TiO_2 (ca. 3.2 eV), is observed for the spectrum of $\beta\text{-NaYF}_4\text{:Yb}^{3+},\text{Tm}^{3+}@\text{SiO}_2@\text{TiO}_2$.¹⁶ This phenomenon indicates that the outer TiO_2 layer plays a significant role in affecting the light absorption property of $\beta\text{-NaYF}_4\text{:Yb}^{3+},\text{Tm}^{3+}@\text{SiO}_2@\text{TiO}_2$ double-shell-structured upconversion photocatalyst. More importantly, the absorption intensity of the outer TiO_2 layer is enhanced compared to that of P25, indicating the extension of the light responsive range.^{26–28} Combining the information given by the three samples, we can conclude that the light absorption range of the TiO_2 shell is extended to ca. 828 nm. The origination of the

light absorption extension can be illustrated by the N 1s and F 1s XPS analysis shown in Figure 3a,b, respectively (Notice: the

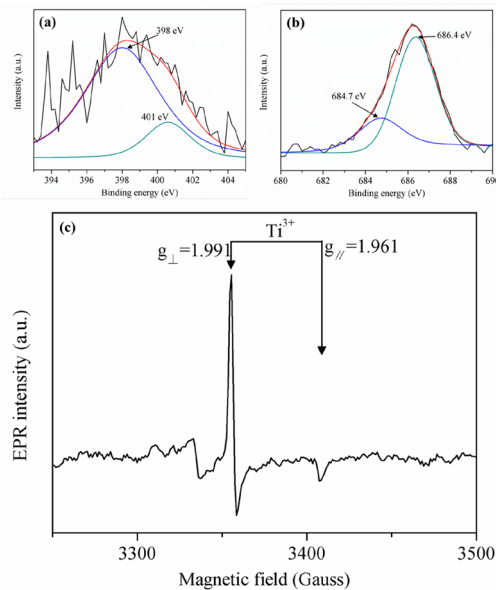


Figure 3. (a) N 1s, (b) F 1s high resolution XPS spectra, and (c) typical Ti^{3+} EPR signal of $\beta\text{-NaYF}_4\text{:Yb}^{3+},\text{Tm}^{3+}\text{@SiO}_2\text{@TiO}_2$.

investigation depth is less than 10 nm; thus, the results can be ascribed to be originated from the outer TiO_2 shell). Two XPS peaks of N 1s signal centered at 398 and 401 eV can be ascribed to the intersectional N species located in the TiO_2 lattice, which will enhance the light absorption in the visible range.^{10,29} The F 1s XPS peak with an asymmetric shape is also detected. The existence of the surface absorbed F atoms (with peak centered at 684.7 eV) will reduce the surface energy of TiO_2 particles, resulting in preferential growth of the crystals exposed with the high-reactive {001} facets.³⁰ The F 1s peak centered at 686.4 eV can be ascribed to the substitution F atoms with Ti–F–Ti chemical bonds, which will result in the formation of Ti^{3+} centers to extend the TiO_2 light absorption to the NIR range.³¹ To further confirm the existence of Ti^{3+} centers, EPR analysis was conducted. In Figure 3c, a typical Ti^{3+} signal with g values of $g_{\perp} = 1.99$ and $g_{\parallel} = 1.96$ was observed in the sample of $\beta\text{-NaYF}_4\text{:Yb}^{3+},\text{Tm}^{3+}\text{@SiO}_2\text{@TiO}_2$. The formation of Ti^{3+} in TiO_2 nanocrystals exposed with the {001} facets in such a critical environment with the presence of F atoms may due to the high pressure. The high pressure may promote the substitution of O by the F atoms. A similar result has been reported by our group in the preparation of pure anatase TiO_2 nanosheets.¹⁰

Photoluminescence spectra of $\beta\text{-NaYF}_4\text{:Yb}^{3+},\text{Tm}^{3+}$, $\beta\text{-NaYF}_4\text{:Yb}^{3+},\text{Tm}^{3+}\text{@SiO}_2$, and $\beta\text{-NaYF}_4\text{:Yb}^{3+},\text{Tm}^{3+}\text{@SiO}_2\text{@TiO}_2$ are shown in Figure 2b to illustrate whether the photo energy generated via the upconversion process by UCPs can be absorbed by the high-reactive TiO_2 layer. The emitted upconversion luminescence was conducted under the excitation of the 980 nm laser beam. Bright blue light with emission bands centered at 288, 360, 449, 474, 645, and 695 nm of $\beta\text{-NaYF}_4\text{:Yb}^{3+},\text{Tm}^{3+}$ (inset in Figure 2b (left)) can be observed by the naked eye. The luminescence intensity of $\beta\text{-NaYF}_4\text{:Yb}^{3+},\text{Tm}^{3+}\text{@SiO}_2$ decreased a little compared to that of pure $\beta\text{-NaYF}_4\text{:Yb}^{3+},\text{Tm}^{3+}$. However, the coated SiO_2 shell with hydrophilic property will improve the dispersion condition in the aqueous solutions so as to enhance the contact between the

pollutants and as-prepared upconversion photocatalysts.³² This layer will also prevent the HF corrosion during the hydrothermal process and electron trapping caused by surface defects and ligands of bare $\beta\text{-NaYF}_4\text{:Yb}^{3+},\text{Tm}^{3+}$.²¹ Furthermore, the photocatalytic process undergoes complicated reduction and oxidation reactions, and the introduction of SiO_2 will also prevent the upconversion particle from photocatalysis induced corrosion to prolong its lifetime. Therefore, coating with SiO_2 would not result in heavy attenuation of the upconversion photocatalytic activity. After further TiO_2 coating, the luminescence intensity decreased significantly compared to that of $\beta\text{-NaYF}_4\text{:Yb}^{3+},\text{Tm}^{3+}\text{@SiO}_2$. The significant decrement appearing here can be illustrated by the part of the emitted luminescence that has been absorbed by the TiO_2 shell, for the emission bands are all in the absorption range of the TiO_2 shell.¹⁶ More importantly, the full spectrum decrement confirms that the TiO_2 shell can absorb the long wavelength light. This is very different from the already reported results in which the photocatalysts can only make use of the UV for photocatalysis.^{16,17} Due to the scattering effect (*this effect will also decrease the NIR intensity only a little according to the published works*^{16,17}) of TiO_2 nanocrystals, the upconverted luminescence will irradiate a larger area compared to the single light path of pure $\beta\text{-NaYF}_4\text{:Yb}^{3+},\text{Tm}^{3+}$ dispersed in cyclohexane (inset in Figure 2b). These efficient energy transfer processes will be beneficial for NIR-driven photocatalysis.

To find out the effect of different UCPs played on photocatalytic activities of the new kind upconversion photocatalyst, $\beta\text{-NaYF}_4\text{:Yb}^{3+},\text{Er}^{3+}$ with different emission bands was also employed as the core material to compare with that of the $\beta\text{-NaYF}_4\text{:Yb}^{3+},\text{Tm}^{3+}$ -based upconversion photocatalyst. As shown in Figure 2c,d, a similar phenomenon is observed for $\beta\text{-NaYF}_4\text{:Yb}^{3+},\text{Er}^{3+}$ -based samples, except the emitted blue luminescence was replaced by the bright green luminescence which has emission bands centered at 380, 407, 522, 548, and 660 nm. Comparing the luminescence wavelength of $\beta\text{-NaYF}_4\text{:Yb}^{3+},\text{Tm}^{3+}$ and $\beta\text{-NaYF}_4\text{:Yb}^{3+},\text{Er}^{3+}$, it is clear that the luminescence derived from $\beta\text{-NaYF}_4\text{:Yb}^{3+},\text{Tm}^{3+}$ has higher photo energy which is very beneficial for photocatalytic reactions in decomposing pollutants. Furthermore, the luminescence intensity of $\beta\text{-NaYF}_4\text{:Yb}^{3+},\text{Er}^{3+}$ is three times higher than that of $\beta\text{-NaYF}_4\text{:Yb}^{3+},\text{Tm}^{3+}$, which may due to the different percentage of the doped rare earth ions. On the basis of our previous studies, the constitutions of both samples are the optimal ones to give the highest luminescence intensity.³³ More importantly, the upconversion process from Yb^{3+} to Er^{3+} is a two-step process, while the one from Yb^{3+} to Tm^{3+} is a three- or four-step process.³⁴ Thus, the probability of the first one is normally higher. Moreover, the Yb^{3+} to Er^{3+} energy transfer is a resonant one, while Yb^{3+} to Tm^{3+} is a nonresonant one, meaning that extra energy from the crystal lattice is needed to have upconversion in the latter case. This also will make Tm^{3+} emissions weaker through upconversion compared to that of Er^{3+} . Anyway, the same particle size of $\beta\text{-NaYF}_4\text{:Yb}^{3+},\text{Tm}^{3+}$ and $\beta\text{-NaYF}_4\text{:Yb}^{3+},\text{Er}^{3+}$ shown in Figure S1, Supporting Information, may allow us to exclude the particle size effect and only consider the luminescence intensity and photon energy effects on the photocatalytic reactions.

3.3. Photocatalytic Activity Measurement. On the basis of the above results, we tested the photocatalytic activity of $\beta\text{-NaYF}_4\text{:Yb}^{3+},\text{Tm}^{3+}$ - and $\beta\text{-NaYF}_4\text{:Yb}^{3+},\text{Er}^{3+}$ -based upconversion photocatalysts with double-shell structures for the photocatalytic degradation of RhB under the NIR irradiation (15 W/

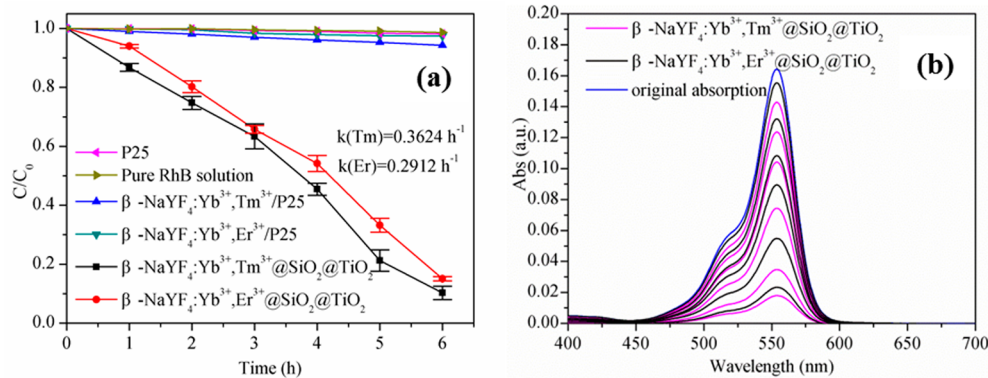


Figure 4. (a) Photocatalytic activities and first order apparent rate constants of as-prepared photocatalysts in the degradation of RhB under the NIR (980 nm, 15 W/mm²) irradiation and (b) corresponding RhB absorption spectra at the initial state and with the presence of $\beta\text{-NaYF}_4\text{:Yb}^{3+},\text{Tm}^{3+}@{\text{SiO}_2@{\text{TiO}}_2}$ and $\beta\text{-NaYF}_4\text{:Yb}^{3+},\text{Er}^{3+}@{\text{SiO}_2@{\text{TiO}}_2}$.

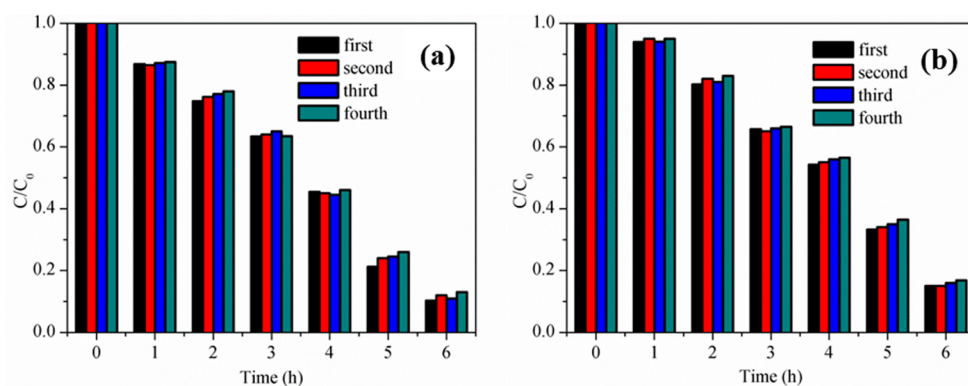


Figure 5. Repeated photocatalytic activity measurements with the presence of (a) $\beta\text{-NaYF}_4\text{:Yb}^{3+},\text{Tm}^{3+}@{\text{SiO}_2@{\text{TiO}}_2}$ and (b) $\beta\text{-NaYF}_4\text{:Yb}^{3+},\text{Er}^{3+}@{\text{SiO}_2@{\text{TiO}}_2}$ under the 980 nm laser (15 W/mm²) irradiation.

mm²). Photocatalytic activities of pure P25/TiO₂ and their physical mixture with $\beta\text{-NaYF}_4\text{:Yb}^{3+},\text{Tm}^{3+}/\text{Er}^{3+}$ were also tested. Figure 4a gives the RhB photodecomposition efficiency curves as a function of the irradiation time with the presence of as-prepared photocatalysts under the NIR irradiation. It can be observed that pure RhB aqueous solution shows little degradation in 6 h, indicating its stability under such an intense laser irradiation. With the presence of $\beta\text{-NaYF}_4\text{:Yb}^{3+},\text{Tm}^{3+}$ and $\beta\text{-NaYF}_4\text{:Yb}^{3+},\text{Er}^{3+}$, the absorption intensity of RhB at 553 nm decreases gradually with the increase of irradiation time (Figure 4b), indicating the degradation of RhB under the NIR irradiation is ascribed to the photocatalytic reaction of the photocatalysts.³⁵ The photocatalytic degradation efficiency was evaluated through the concentration after NIR irradiation relative to the original absorption value of RhB. It is observed that the photocatalytic activity of $\beta\text{-NaYF}_4\text{:Yb}^{3+},\text{Tm}^{3+}@{\text{SiO}_2@{\text{TiO}}_2}$ is higher than that of $\beta\text{-NaYF}_4\text{:Yb}^{3+},\text{Er}^{3+}@{\text{SiO}_2@{\text{TiO}}_2}$. The first order apparent rate constant increased from 0.2912 h^{-1} ($k(Er)$) to 0.3624 h^{-1} ($k(Tm)$) with the replacement of $\beta\text{-NaYF}_4\text{:Yb}^{3+},\text{Er}^{3+}@{\text{SiO}_2@{\text{TiO}}_2}$ by $\beta\text{-NaYF}_4\text{:Yb}^{3+},\text{Tm}^{3+}@{\text{SiO}_2@{\text{TiO}}_2}$. As discussed, the luminescence intensity of $\beta\text{-NaYF}_4\text{:Yb}^{3+},\text{Er}^{3+}@{\text{SiO}_2@{\text{TiO}}_2}$ is higher than that of $\beta\text{-NaYF}_4\text{:Yb}^{3+},\text{Tm}^{3+}@{\text{SiO}_2@{\text{TiO}}_2}$; the higher photocatalytic activity of $\beta\text{-NaYF}_4\text{:Yb}^{3+},\text{Tm}^{3+}@{\text{SiO}_2@{\text{TiO}}_2}$ may indicate that the emission bands position of upconversion materials are more important for their photocatalytic activity. This result can also be proven by P25-based upconversion composites. The composite of $\beta\text{-NaYF}_4\text{:Yb}^{3+},\text{Tm}^{3+}/\text{P25}$ gives more decomposition of RhB than

that of $\beta\text{-NaYF}_4\text{:Yb}^{3+},\text{Er}^{3+}/\text{P25}$ and pure P25 under the NIR irradiation. Another interesting point is how the TiO₂ make uses of the low frequency emissions for efficient photocatalysis. As is known, TiO₂ photosensitized by RhB may give itself visible-light-driven photocatalytic activity.³⁶ In the present study, the UV emissions are much weaker than the visible ones. However, such intense visible emissions did not give $\beta\text{-NaYF}_4\text{:Yb}^{3+},\text{Tm}^{3+}/\text{P25}$ and $\beta\text{-NaYF}_4\text{:Yb}^{3+},\text{Er}^{3+}/\text{P25}$ higher photocatalytic activity compared to the composites of $\beta\text{-NaYF}_4\text{:Yb}^{3+},\text{Tm}^{3+}/\text{Er}^{3+}$ and TiO₂ nanocrystals (Figure S4, Supporting Information). This result may allow us to ascribe the use of the low frequency emissions for photocatalysis to the introduced N and Ti³⁺ species, and it is true that a lot of works have confirmed that N and/or Ti³⁺ doping can improve the visible-light photocatalytic activity of TiO₂. Moreover, it also indicates the importance of close contact between the photocatalysts and UCPs in the preparation of the NIR-driven photocatalysts.

To investigate the durability of their photocatalytic activities under the NIR irradiation, we repeat the same photocatalytic degradation test of $\beta\text{-NaYF}_4\text{:Yb}^{3+},\text{Tm}^{3+}@{\text{SiO}_2@{\text{TiO}}_2}$ for four cycles (Figure 5). As can be observed, the NIR-driven photocatalytic activity of $\beta\text{-NaYF}_4\text{:Yb}^{3+},\text{Tm}^{3+}@{\text{SiO}_2@{\text{TiO}}_2}$ is very stable. As is known, the irradiated light intensity also plays a significant role in affecting the photocatalytic activity. Hence, photocatalytic degradation of RhB was also conducted under the NIR irradiation with different power density. It can be observed from Figure 6 that the photocatalytic activity is increased with the increment of NIR power density, due to the

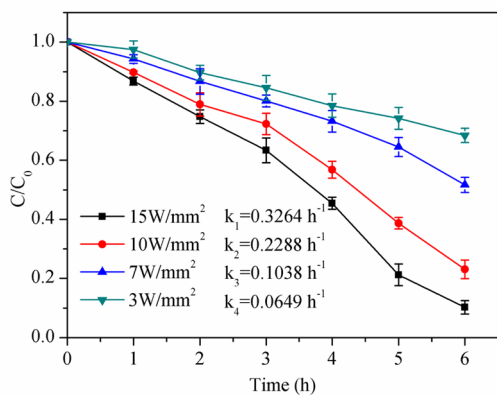


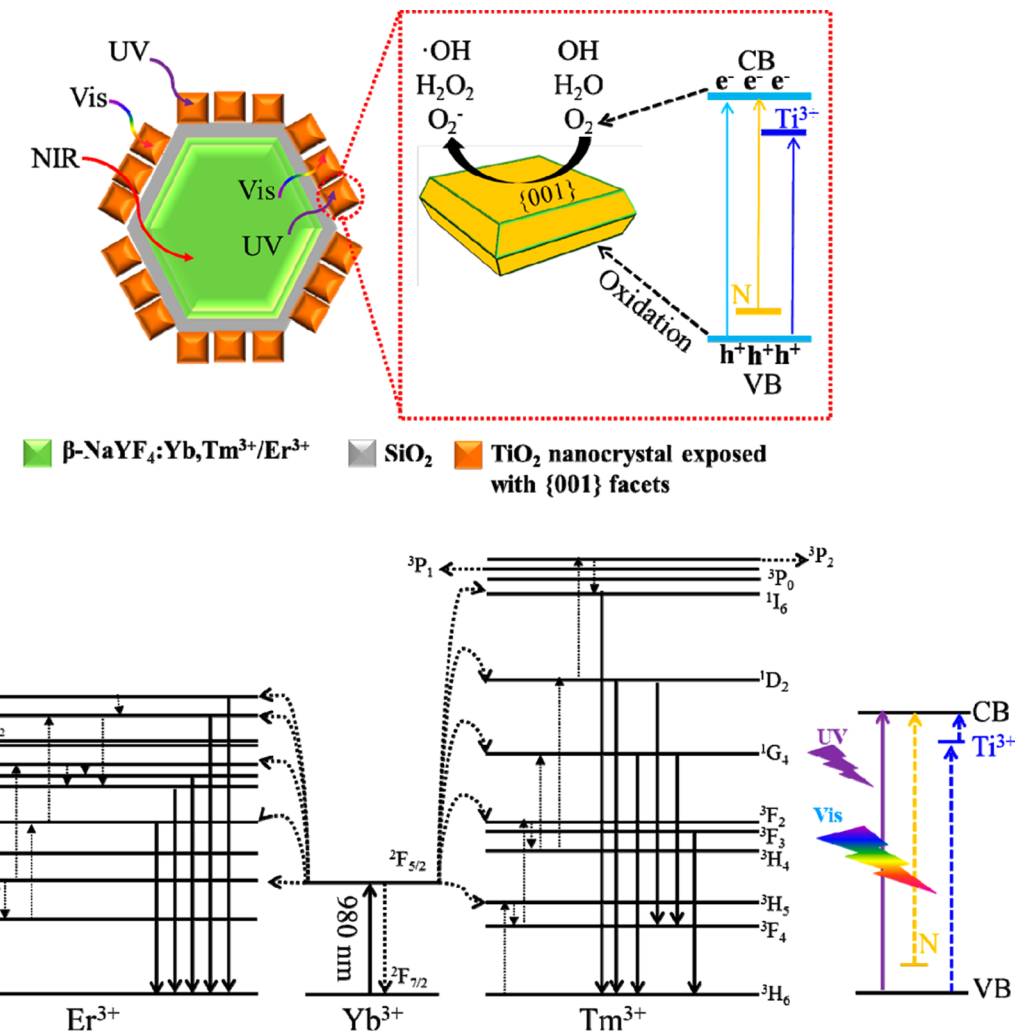
Figure 6. Photocatalytic activities and first order apparent rate constants of $\beta\text{-NaYF}_4\text{:Yb}^{3+},\text{Tm}^{3+}\text{@SiO}_2\text{@TiO}_2$ in the degradation of RhB under the NIR (980 nm) irradiation with different power densities.

upconversion efficiency of $\beta\text{-NaYF}_4\text{:Yb}^{3+},\text{Tm}^{3+}$ being closely related to the excitation light intensity. The first order apparent order constants also show great differences among each other. This phenomenon may allow us to get a new idea to make use

of the NIR energy of the sunlight for photocatalysis. In fact, different power intensities will give different thermal effects; the already published work and our results have confirmed that thermal effect has little influence on the degradation of this type of organic pollutant.¹⁶

In order to confirm the superiority of $\beta\text{-NaYF}_4\text{:Yb}^{3+},\text{Tm}^{3+}$ over $\beta\text{-NaYF}_4\text{:Yb}^{3+},\text{Er}^{3+}$ in improving the NIR-driven photocatalytic activity, UV and visible light were also employed as the light sources to investigate the photocatalytic activity. As shown in Figure S5, Supporting Information, both $\beta\text{-NaYF}_4\text{:Yb}^{3+},\text{Tm}^{3+}\text{@SiO}_2\text{@TiO}_2$ and $\beta\text{-NaYF}_4\text{:Yb}^{3+},\text{Er}^{3+}\text{@SiO}_2\text{@TiO}_2$ give similar degradation of RhB under the visible light irradiation. A slight cross of the photocatalytic results may result from the experimental operation during the photocatalytic process. P25-based photocatalytic composites have little effect on the degradation of RhB, confirming that the visible-light-driven property of as-prepared double-shell-structured photocatalysts is due to the introduction of N and Ti³⁺ and the significant role of the NIR applied in photocatalysis. When the UV light was employed as the excitation source (Figure S6, Supporting Information), P25 gave the highest decomposition compared to the rest of the photocatalysts. The lower decomposition of $\beta\text{-NaYF}_4\text{:Yb}^{3+},\text{Tm}^{3+}/\text{P25}$ and $\beta\text{-}$

Scheme 2. Photocatalytic Mechanisms of $\beta\text{-NaYF}_4\text{:Yb}^{3+},\text{Tm}^{3+}/\text{Er}^{3+}\text{@SiO}_2\text{@TiO}_2$ Upconversion Photocatalysts under the Full Spectrum Light Irradiation and Upconversion Mechanisms of $\beta\text{-NaYF}_4\text{:Yb}^{3+},\text{Tm}^{3+}/\text{Er}^{3+}$ under the 980 nm Laser Irradiation



$\text{NaYF}_4\text{:Yb}^{3+},\text{Er}^{3+}/\text{P2S}$ may due to the disturbance of light absorption by $\beta\text{-NaYF}_4\text{:Yb}^{3+},\text{Tm}^{3+}$ and $\beta\text{-NaYF}_4\text{:Yb}^{3+},\text{Er}^{3+}$, for they were just physically mixed together. More importantly, $\beta\text{-NaYF}_4\text{:Yb}^{3+},\text{Tm}^{3+}@\text{SiO}_2@\text{TiO}_2$ and $\beta\text{-NaYF}_4\text{:Yb}^{3+},\text{Er}^{3+}@\text{SiO}_2@\text{TiO}_2$ also show similar photocatalytic activity in the degradation of RhB. The similar photocatalytic results under the UV and visible light irradiation indicate that both $\beta\text{-NaYF}_4\text{:Yb}^{3+},\text{Tm}^{3+}@\text{SiO}_2@\text{TiO}_2$ and $\beta\text{-NaYF}_4\text{:Yb}^{3+},\text{Er}^{3+}@\text{SiO}_2@\text{TiO}_2$ have almost the same structures which have little effect on comparing their photocatalytic activity. These results may allow us to confirm the superior photocatalytic activity of $\beta\text{-NaYF}_4\text{:Yb}^{3+},\text{Tm}^{3+}@\text{SiO}_2@\text{TiO}_2$ to $\beta\text{-NaYF}_4\text{:Yb}^{3+},\text{Er}^{3+}@ \text{SiO}_2@\text{TiO}_2$ under the NIR irradiation to $\beta\text{-NaYF}_4\text{:Yb}^{3+},\text{Tm}^{3+}$ which can upconvert the NIR to higher energy photons more efficiently than $\beta\text{-NaYF}_4\text{:Yb}^{3+},\text{Er}^{3+}$. One more thing that should be pointed out is the UV-driven photocatalytic activity of the double-shell-structured photocatalysts being higher than that of the P2S composites, indicating the superiority of the structure due to the TiO_2 nanocrystals being all deposited on the outer shell. Further work may be needed to improve the photocatalytic activity of the TiO_2 shell.

Scheme 2 gives a deep insight on $\beta\text{-NaYF}_4\text{:Yb}^{3+},\text{Tm}^{3+}@ \text{SiO}_2@\text{TiO}_2$ and $\beta\text{-NaYF}_4\text{:Yb}^{3+},\text{Er}^{3+}@ \text{SiO}_2@\text{TiO}_2$ absorbing the full spectrum of light for photocatalysis. The outer TiO_2 layer can quickly absorb the UV and visible light for photocatalysis, for its intrinsic property and its bandgap modification by N and Ti^{3+} species. The high penetrability of the NIR allows it to go further into the inner structure to excite the upconversion materials, such as $\beta\text{-NaYF}_4\text{:Yb}^{3+},\text{Tm}^{3+}$ and $\beta\text{-NaYF}_4\text{:Yb}^{3+},\text{Er}^{3+}$. The pumping of 980 nm of light only excites the Yb^{3+} ion, resulting in population of the $^2\text{F}_{5/2}$ level. Then, the Tm^{3+} and Er^{3+} ions will be excited due to the efficient energy transfer from Yb^{3+} . For the sample of $\beta\text{-NaYF}_4\text{:Yb}^{3+},\text{Tm}^{3+}$, the emitted light centered at 288, 360, 449, 474, 645, and 695 nm is attributed to the Tm^{3+} transitions of $^1\text{I}_6\rightarrow^3\text{H}_6$, $^1\text{D}_2\rightarrow^3\text{H}_6$, $^1\text{D}_2\rightarrow^3\text{F}_4$, $^1\text{G}_4\rightarrow^3\text{H}_6$, $^1\text{G}_4\rightarrow^3\text{F}_4$, and $^3\text{F}_3\rightarrow^3\text{H}_6$. The emission peaks centered at 380, 407, 522, 548, and 660 nm of $\beta\text{-NaYF}_4\text{:Yb}^{3+},\text{Er}^{3+}$ are attributed to the Er^{3+} transitions of $^4\text{G}_{11/2}\rightarrow^4\text{I}_{15/2}$, $^2\text{H}_{9/2}\rightarrow^4\text{I}_{15/2}$, $^2\text{H}_{11/2}\rightarrow^4\text{I}_{15/2}$, $^4\text{S}_{3/2}\rightarrow^4\text{I}_{15/2}$, and $^4\text{F}_{9/2}\rightarrow^4\text{I}_{15/2}$. It is clear that the Tm^{3+} and Er^{3+} give different properties in converting the NIR to high energy photons, which affects the NIR-driven photocatalysis significantly. Furthermore, these emission peaks are all in the UV and visible range, which are totally in the TiO_2 absorption range. Then, the upconverted light will go through the transparent SiO_2 layer to excite the outer high-reactive TiO_2 nanocrystals. By all these steps, the as-prepared upconversion photocatalysts can absorb the NIR efficiently for photocatalysis. The $\{001\}$ facets of TiO_2 nanocrystals will also enhance the photocatalytic activity to a certain degree. We also tried to etch the SiO_2 layer to get a higher intensity of the upconverted luminescence. However, the TiO_2 nanocrystals will depart from the particles, for they are rooting on the SiO_2 shell (Figure S7, Supporting Information). Heat treating the particles may allow the TiO_2 nanocrystals to form a compact shell, but this will cause the elimination of the $\{001\}$ facets and will decrease the specific surface area of the photocatalysts which are negative for photocatalytic activity enhancement.^{37,38} These topics may be very promising in the near future.

4. CONCLUSIONS

In this work, for the first time, highly uniform double-shell-structured $\beta\text{-NaYF}_4\text{:Yb}^{3+},\text{Tm}^{3+}/\text{Er}^{3+}@ \text{SiO}_2@\text{TiO}_2$ photocatalysts were prepared and employed for RhB degradation. The designed structure gives effective energy transfer from UCPs to TiO_2 . Similar photocatalytic activity of $\beta\text{-NaYF}_4\text{:Yb}^{3+},\text{Tm}^{3+}@ \text{SiO}_2@\text{TiO}_2$ and $\beta\text{-NaYF}_4\text{:Yb}^{3+},\text{Er}^{3+}@ \text{SiO}_2@\text{TiO}_2$ under the UV and visible light irradiation confirms their similar structures. The superior photocatalytic activity of $\beta\text{-NaYF}_4\text{:Yb}^{3+},\text{Tm}^{3+}@ \text{SiO}_2@\text{TiO}_2$ over $\beta\text{-NaYF}_4\text{:Yb}^{3+},\text{Er}^{3+}@ \text{SiO}_2@\text{TiO}_2$ under the NIR irradiation gives us a new insight on enhancing the upconversion photocatalytic activity by proper UCPs which can emit higher energy photons. Furthermore, the NIR-driven photocatalytic activity is very stable and is closely related to the NIR power density. Our work paves an effective way to enable the application of NIR energy for photocatalysis by employing UCPs. Further improvement of performance for photocatalysis based on upconversion materials and TiO_2 might be achieved by enhancing the upconversion fluorescence of UCPs by various means, controlling the thickness of SiO_2 and TiO_2 , and enhancing the photocatalytic activity of TiO_2 by noble metals and high-conductive materials modification.

■ ASSOCIATED CONTENT

■ Supporting Information

SEM images of $\beta\text{-NaYF}_4\text{:Yb}^{3+},\text{Tm}^{3+}$ and $\beta\text{-NaYF}_4\text{:Yb}^{3+},\text{Er}^{3+}$, TEM images of $\beta\text{-NaYF}_4\text{:Yb}^{3+},\text{Er}^{3+}@ \text{SiO}_2@\text{TiO}_2$, XRD diffraction spectra of $\beta\text{-NaYF}_4\text{:Yb}^{3+},\text{Er}^{3+}$ -based samples, supplementary photocatalytic results of the samples under the UV, vis, and NIR irradiation, and TEM image of $\beta\text{-NaYF}_4\text{:Yb}^{3+},\text{Tm}^{3+}@ \text{SiO}_2@\text{TiO}_2$ after NaOH etching. This material is available free of charge via the Internet at <http://pubs.acs.org>.

■ AUTHOR INFORMATION

Corresponding Authors

*Fax: +86-25-83587220. Tel: +86-25-83587252. E-mail: wwnjut@hotmail.com (W.W.).

*Fax: +86-25-83587220. Tel: +86-25-83587252. E-mail: lchnjut@163.com (C.L.).

Notes

The authors declare no competing financial interest.

■ ACKNOWLEDGMENTS

This work was supported by the National Natural Science Foundation of China (Grant No. 20901040/B0111), the Key University Science Research Project of Jiangsu Province (No. 10KJA430016), and a project funded by the Priority Academic Program Development of Jiangsu Higher Education Institutions (PAPD).

■ REFERENCES

- (1) Chen, C.; Ma, W.; Zhao, J. *Chem. Soc. Rev.* **2010**, *39*, 4206–4219.
- (2) Wang, G.; Ling, Y.; Li, Y. *Nanoscale* **2012**, *4*, 6682–6691.
- (3) Fujishima, A.; Zhang, X.; Tryk, D. *Surf. Sci. Rep.* **2008**, *63*, 515–582.
- (4) Fujishima, A.; Honda, K. *Nature* **1972**, *238*, 37–38.
- (5) Ulrike, D. *Surf. Sci. Rep.* **2003**, *48*, 53–229.
- (6) Qin, W.; Zhang, D.; Zhao, D.; Wang, L.; Zheng, K. *Chem. Commun.* **2010**, *64*, 2304–2306.
- (7) Wang, W.; Lu, C. H.; Ni, Y. R.; Su, M. X.; Huang, W. J.; Xu, Z. Z. *Appl. Surf. Sci.* **2012**, *258*, 8696–8703.
- (8) Asahi, R.; Morikawa, T.; Ohwaki, T.; Aoki, K.; Taga, Y. *Science* **2001**, *293*, 269–271.

- (9) Weber, A. S.; Grady, A. M.; Koodali, R. T. *Catal. Sci. Technol.* **2012**, *2*, 683–693.
- (10) Wang, W.; Lu, C. H.; Ni, Y. R.; Su, M. X.; Xu, Z. Z. *Appl. Catal., B: Environ.* **2012**, *127*, 28–35.
- (11) Zheng, Z.; Huang, B.; Meng, X.; Wang, J.; Wang, S.; Lou, Z.; Wang, Z.; Qin, X.; Zhang, X.; Dai, Y. *Chem. Commun.* **2013**, *49*, 868–870.
- (12) Muhich, C. L.; Zhou, Y.; Holder, A. M.; Weimer, A. W.; Musgrave, C. B. *J. Phys. Chem. C* **2012**, *116*, 10138–10149.
- (13) Wang, X.; Liu, G.; Wang, L.; Chen, Z.-G.; Lu, G. Q.; Cheng, H.-M. *Adv. Energy Mater.* **2012**, *2*, 42–46.
- (14) Zhang, J.; Xiong, Z.; Zhao, X. S. *J. Mater. Chem.* **2011**, *21*, 3634–3640.
- (15) Chen, X.; Liu, L.; Yu, P. Y.; Mao, S. S. *Science* **2011**, *331*, 746–750.
- (16) Tang, Y.; Di, W.; Zhai, X.; Yang, R.; Qin, W. *ACS Catal.* **2013**, *3*, 405–412.
- (17) Li, Z.; Li, C.; Mei, Y.; Wang, L.; Du, G.; Xiong, Y. *Nanoscale* **2013**, *5*, 3030–3036.
- (18) Gibart, P.; Auzel, F.; Guillaume, J. C.; Zahraman, K. *Jpn. J. Appl. Phys.* **1996**, *35*, 4401–4402.
- (19) Ren, L.; Qi, X.; Liu, Y.; Huang, Z.; Wei, X.; Li, J.; Yang, L.; Zhong, J. *J. Mater. Chem.* **2012**, *22*, 11765–11771.
- (20) Chen, F.; Bu, W.; Zhang, S.; Liu, J.; Fan, W.; Zhou, L.; Peng, W.; Shi, J. *Adv. Funct. Mater.* **2013**, *23*, 298–307.
- (21) Liang, L.; Liu, Y.; Bu, C.; Guo, K.; Sun, W.; Huang, N.; Peng, T.; Sebo, B.; Pan, M.; Liu, W.; Guo, S.; Zhao, X. Z. *Adv. Mater.* **2013**, *25*, 2174–2180.
- (22) Wang, W.; Lu, C. H.; Ni, Y. R.; Song, J. B.; Su, M. X.; Xu, Z. Z. *Catal. Commun.* **2012**, *22*, 19–23.
- (23) Shen, J.; Zhu, Y.; Yang, X.; Li, C. *J. Mater. Chem.* **2012**, *22*, 13341–13347.
- (24) Yang, H. G.; Sun, C. H.; Qiao, S. Z.; Zou, J.; Liu, G.; Smith, S. C.; Cheng, H. M.; Lu, G. Q. *Nature* **2008**, *453*, 638–641.
- (25) Wen, C. Z.; Jiang, H. B.; Qiao, S. Z.; Yang, H. G.; Lu, G. Q. *J. Mater. Chem.* **2011**, *21*, 7052–7061.
- (26) Wang, W.; Lu, C. H.; Ni, Y. R.; Xu, Z. Z. *CrystEngComm* **2013**, *15*, 2537–2543.
- (27) Wang, W.; Ni, Y. R.; Lu, C. H.; Xu, Z. Z. *RSC Adv.* **2012**, *2*, 8286–8288.
- (28) Barolo, G.; Livraghi, S.; Chiesa, M.; Paganini, M. C.; Giannello, E. *J. Phys. Chem. C* **2012**, *116*, 20887–20894.
- (29) Tian, H.; Hu, L.; Zhang, C.; Liu, W.; Huang, Y.; Mo, L.; Guo, L.; Sheng, J.; Dai, S. *J. Phys. Chem. C* **2010**, *114*, 1627–1632.
- (30) Liu, G.; Yu, J. C.; Lu, G. Q.; Cheng, H. M. *Chem. Commun.* **2011**, *47*, 6763–6765.
- (31) Czoska, A. M.; Livraghi, S.; Chiesa, M.; Giannello, E.; Agnoli, S.; Granozzi, G.; Finazzi, E.; Valentini, C. D.; Pacchioni, G. *J. Phys. Chem. C* **2008**, *112*, 8951–8956.
- (32) Xing, H.; Bu, W.; Zhang, S.; Zheng, X.; Li, M.; Chen, F.; He, Q.; Zhou, L.; Peng, W.; Hua, Y.; Shi, J. *Biomaterials* **2012**, *33*, 1079–1089.
- (33) Huang, W. J.; Lu, C. H.; Jiang, C. F.; Wang, W.; Song, J. B.; Ni, Y. R.; Xu, Z. Z. *J. Colloid Interface Sci.* **2013**, *376*, 34–39.
- (34) Auzel, F. *Chem. Rev.* **2004**, *104*, 139–174.
- (35) Lee, J. S.; You, K. H.; Park, C. B. *Adv. Mater.* **2012**, *24*, 1084–1088.
- (36) Yan, X. L.; Ohno, T.; Nishijima, K.; Abe, R.; Ohtani, B. *Chem. Phys. Lett.* **2006**, *429*, 606–610.
- (37) Xiang, Q.; Yu, J.; Jaroniec, M. *Phys. Chem. Chem. Phys.* **2011**, *13*, 4853–4861.
- (38) Joo, J. B.; Zhang, Q.; Lee, I.; Dahl, M.; Zaera, F.; Yin, Y. *Adv. Funct. Mater.* **2012**, *22*, 166–174.